Ceramics International 46 (2020) 29233–29243

Contents lists available at ScienceDirect

Ceramics International

journal homepage: www.elsevier.com/locate/ceramint

Carbon nanotube-metal oxide nanocomposite gas sensing mechanism assessed via NO_2 adsorption on *n*-WO_3/*p*-MWCNT nanocomposites

Nguyen Manh Hung[a,b], Nguyen Duc Chinh[a], Tien Dai Nguyen[c,d], Eui Tae Kim[a], GyuSeok Choi[e], Chunjoong Kim[a,**], Dojin Kim[a,*]

[a] Department of Materials Science and Engineering, Chungnam National University, Daejeon, 34134, Republic of Korea
[b] Department of Materials Science and Engineering, Le Quy Don Technical University, Hanoi, 100000, Viet Nam
[c] Institute of Theoretical and Applied Research, Duy Tan University, Hanoi, 100000, Viet Nam
[d] Faculty of Natural Sciences, Duy Tan University, Da Nang, 550000, Viet Nam
[e] Gumi Electronic and Information Technology Research Institute, Gumi, Gyeongbuk, 39171, Republic of Korea

ARTICLE INFO

Keywords:
WO_3/MWCNT composite
NO_2 detection
Nano sensor

ABSTRACT

A series of WO_3/multiwalled carbon nanotube (MWCNT) nanocomposite sensors was fabricated by bar-coating slurries using different ratios of MWCNTs to WO_3 nanoparticles. The morphology, composition, and structure of the fabricated nanocomposites were examined using electron microscopy, X-ray diffraction, ultraviolet and X-ray photoelectron spectroscopy, Raman spectroscopy, and nitrogen adsorption-desorption measurements, with the aim of completely identifying the physical and electronic structures of the nanocomposites. The effects of the different ratios of the nanocomposites on the electrical conductance and NO_2 gas sensing properties were examined and compared with the morphological investigation results. The synergetic properties of the nanocomposite sensors were a result of the combined effect of low-doped semiconducting WO_3 and metallic MWCNTs. Because nanoscale sensors exhibit a maximal response on the scale of their depletion depth, individual components with conductivities that are either too low or too high cannot meet the condition. Meanwhile, their mixture can establish the required condition for the maximal response which appears as a synergetic effect. Based on this effect, the optimal nanocomposite sensor (0.5 wt% MWCNT) showed a response of ~18 for 5 ppm NO_2 at 150 °C with short response/recovery times (~87 s /~300 s). The synergetic effect in nanocomposite sensors cannot be explained by the interfacial Schottky barrier model, which has been used for sensors of agglomerated particles.

1. Introduction

Multiwalled carbon nanotube (MWCNT) is one of the popular structural morphologies of carbon nanotubes [1,2]. MWCNTs, as other carbon-based materials such as graphite, graphene and reduced graphene oxide, carbon dots, etc, exhibit interesting and unique properties, such as high electrical conductivity, high mechanical strength, and large specific surface area [3–5]. As an important parameter of MWCNT for use in gas sensors, the specific surface area, which strongly depends on the layer number and diameter, was shown to be in the range of 50–800 m^2/g for the layer number of 2–40 layers [4]. In addition, MWCNTs can be easily produced with an industrial-scale by various methods [6–9]; thus, researchers have explored MWCNTs for diverse applications [10–13]. MWCNTs as nanomaterials are also attractive for use in chemoresistive gas sensors owing to their large surface area; however, thus far, their performance has been relatively poor (weak response), apart from the advantage of low operation temperatures [14].

However, when MWCNTs are combined with metal oxides to form composites for use as gas sensors, enhanced gas sensing performance is observed owing to a synergetic effect, compared with sensors that are made of individual components (i.e., oxide or MWCNT sensors) [15–20]. To explain the observed enhanced sensing performance, various aspects of nanomorphological and electronic properties of the composites, related to the MWCNT mixing, have been suggested. Among the most frequently provided explanations are the large surface area of MWCNTs (leading to enhanced molecular adsorption) [18–20], enhanced structural porosity that promotes gas penetration for

* Corresponding author.
** Corresponding author.
E-mail addresses: ckim0218@cnu.ac.kr (C. Kim), dojin@cnu.ac.kr (D. Kim).

https://doi.org/10.1016/j.ceramint.2020.08.097
Received 2 June 2020; Received in revised form 30 July 2020; Accepted 13 August 2020
Available online 22 August 2020

enhanced adsorption [18–21], high electrical conductivity of MWCNTs that increases the carrier supply rate to the receptors' surfaces (and vice versa) [17,20], formation of the *p–n* junction depletion layer [16,18] and related conductivity changes [20], and formation of the Schottky junction and related interfacial potential barrier modulation [19,21]. Although they all relate to the important characteristics of carbon nanotube (CNT) composites, the above-listed proposals do not explain how in fact the listed mechanisms alter the sensing performance of nanocomposites. To the best of our knowledge, only a few systematic investigations have been performed to provide quantitative and/or logical evidence for the above-mentioned claims.

We have examined several CNT-oxide nanocomposite sensor structures [7,22]. The investigated parameters were the nanostructural morphologies related to the synthesis methods, the doping types and concentrations of the oxides, the oxide/CNT ratio modifying the conduction type and transport mechanism in the nanocomposites, transport kinetics and quantitative evaluation of charge exchange upon gas adsorption/desorption. In this article, we summarize our previous studies using a series of WO_3/MWCNT nanocomposite structures with different WO_3/MWCNT ratios. In particular, we elucidate the general operational principle in the nanocomposite sensors of CNTs and metal oxide upon the adsorption of NO_2 gas molecules. We quantitatively examine the origin of the synergetic sensing effect in various CNT/oxide composites.

2. Experiments

2.1. Materials

The reagents, sodium tungstate dihydrate ($Na_2WO_4{\cdot}2H_2O$, ≥ 99 %), nickel (II) chloride hexahydrate ($NiCl_2{\cdot}6H_2O$), ≥ 97 %), nitric acid (HNO_3, 70 %), and dimethylformamide ($HCON(CH_3)_2$, 99.8%), were purchased from Sigma-Aldrich Co., Ltd (USA). MWCNTs were purchased from NanoKarbon Co., Ltd (Korea). All received reagents were used without further purification.

2.2. Fabrication of WO_3/MWCNT nanocomposites

WO_3 powder was synthesized using a conventional hydrothermal method [23]. $Na_2WO_4{\cdot}2H_2O$ (0.025 M) and $NiCl_2{\cdot}6H_2O$ (0.025 M) were each dissolved in 60 ml H_2O and stirred for 30 min to form homogeneous solutions. The two solutions were combined using vigorous stirring for 10 min to produce a uniform green solution. The mixture was transferred to a Teflon-lined stainless steel autoclave and heated at 160 °C for 24 h. The reaction can be described as following [24,25]:

$$Na_2WO_4 + NiCl_2 \rightarrow NiWO_4 + 2NaCl + H_2O \quad (1)$$

A precipitate of $NiWO_4$ was obtained after the autoclave cooled to room temperature (~25 °C) and was thoroughly cleaned in water and absolute ethanol using the centrifugation method. The precipitate was dried at 70 °C for 24 h to obtain a green powder product. The green powder product was immersed in 4 M HNO_3 and stirred at room temperature for 24 h until the color of corresponding suspension completely changed from green to yellow. The formation of WO_3 can be described by reactions [26]:

$$NiWO_4 + HNO \rightarrow H_2WO_4 + NiNO_3 \quad (2)$$

$$H_2WO_4 \rightarrow WO_3 + H_2O \quad (3)$$

The yellow WO_3 powder obtained via the centrifugation of the suspension was rinsed thoroughly with deionized water and absolute ethanol to remove any contaminants. Finally, the powder was dried at 80 °C for 24 h, followed by annealing at 550 °C for 2 h in air, to obtain a yellow WO_3 powder.

WO_3/MWCNT nanocomposite materials were prepared by mixing the synthesized WO_3 powder and commercial MWCNTs in a dimethylformamide solvent using different WO_3/MWCNT ratios. The mixture slurries were sonicated for 30 min to disperse the MWCNTs in the slurries. To fabricate WO_3/MWCNT nanocomposite sensors, the slurries were bar-coated onto alumina substrates patterned with gold electrodes, followed by drying at 120 °C for 2 h to remove the solvent, as illustrated in Fig. 1a. Finally, the sensor structures were calcined at 400 °C in air for 2 h to eliminate amorphous carbon and enhance the contact between WO_3 and MWCNTs. For reference, pure WO_3 and MWCNT sensors were also fabricated using similar processes. The amounts of MWCNTs in the fabricated sensors were zero (WO_3 sensor), 0.25, 0.5, 1, 5, and 100 wt% (MWCNT sensors). The weight percent values correspond to volume percentage values of 4.6, 8.8, 16.3, and 50.4, respectively, which were calculated by assuming a molecular weight of 231.84 for WO_3 and 12.01 for C. The fabricated composite sensors were labeled W, S1, S2, S3, S4, and M, respectively (Fig. S1, Supporting Information).

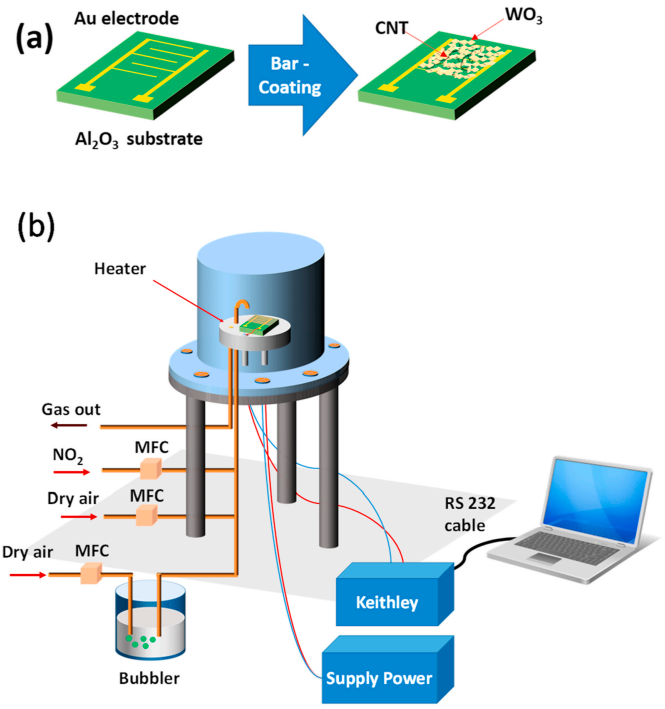

Fig. 1. (a) Schematic of the sensor fabrication process and (b) the setup for gas sensing property measurements.

2.3. Characterization

The morphologies and crystalline structures of the fabricated gas sensing structures were investigated using a field-emission scanning electron microscopy (FESEM) (JSM-700F JEOL, Japan), transmission electron microscopy (TEM) (JEM-ARM 200F, JEOL, Japan), and an X-ray diffraction (XRD) (X'pert PRO-MPD, PANalytical, Netherlands) with Cu-Kα radiation source (λ = 0.15406 nm). The compositions of the samples were examined by energy dispersive spectroscopy (EDS) integrated with the scanning electron microscopy (SEM). The structures of the samples were investigated using Raman spectroscopy with an excitation wavelength of 532 nm at room temperature. In addition, X-ray photoelectron spectroscopy (XPS) (VG Multilab 2000, ThermoVG Scientific, UK) measurements were also obtained to determine the chemical state of W in WO_3 and the WO_3/MWCNT nanocomposites. The binding energy of C 1s from adventitious carbon (284.8 eV) was used for calibrating the XPS binding energies. The Brunauer–Emmett–Teller (BET) specific surface areas of the composite structures were calculated from the N_2 adsorption-desorption curves using the BET theory. All the studied samples were outgassed at 200 °C for 5 h before the BET measurements were obtained. The work

functions of WO_3 and MWCNTs were measured using ultraviolet photoelectron spectroscopy (UPS) (K-Alpha, Thermo Fisher Scientific Solutions Co., Ltd.) with a He I source with an excitation energy of 21.22 eV. To observe the cutoff regions of secondary electrons in the UPS spectra, bias voltages of 5 and 10 V were applied for MWCNTs and WO_3, respectively. For each of the studied samples, the work function (Φ) was calculated from the binding energy of the Fermi edge (E_F) and from the cutoff energy level of secondary electrons ($E_{cut\ off}$) using the following equation:

$$\Phi = 21.22 - |E_{cut\ off} - E_F| \quad (4)$$

The values of E_F and $E_{cut\ off}$ were determined directly from the respective UPS spectra using the UPS equipment. All the related analyses were performed on the W and S2 samples, unless otherwise specified.

2.4. Gas sensing property measurements

The setup for gas sensing measurements is shown schematically in Fig. 1b [27–29]. The sensors were placed on a substrate plate in an ambient controllable chamber. The sensor temperature was controlled by a resistance heater inserted in the substrate plate. The flow rates of the gases flowing into the chamber were controlled by mass flow controllers. To ensure the gas pressure stability in the chamber, the total gas flux was fixed at 400 sccm, while the target gas concentration, C (ppm), was determined using the formula C (ppm) = C_o (ppm) × f/(f + F), where C_o is the concentration of the target gas in the cylinder, and f and F are the flow rates of the target gas and dry air, respectively. The response of the sensor (S) was calculated as R_g/R_o for oxidizing gases or R_o/R_g for reducing gases, where R_o is the resistance of the sensor in dry air and R_g is that under the target gas flow. In order to evaluate the effect of humidity on the sensor, water-saturated air flow (wet air) was prepared with a bubbler. Each desired relative humidity (RH) value can be formed by mixing the wet air and dry air flows with suitable ratios using MFCs. The real value of RH in the measuring chamber was confirmed by a commercial humidity sensor -Testo 635.

3. Results and discussion

3.1. Morphology and structure

The synthesized WO_3 powder exhibited a morphology of uniform 100-nm-size thick flakes, with the average edge length of a few micrometers and smooth surfaces (Fig. 2a). However, the synthesized WO_3 flakes broke into tiny particles and much smaller flakes after sonication (Fig. 2b–f). SEM images also indicated that MWCNTs were well-dispersed throughout the WO_3 matrix, to form random composite structures. The color of the composite slurries changed from yellow to black as the MWCNTs concentration increased (Fig. S1, Supporting Information). The morphology of raw MWCNTs is shown in Fig. S2, suggesting the 30–100 nm range of diameters, with lengths of up to a few micrometers (Fig. 2g). The EDS spectrum of S2 (Fig. 2h) further illustrates the constituents in the WO_3/MWCNT composites.

The TEM images presented in Fig. 3a and **b** were obtained for the WO_3/MWCNT composites (S2) fabricated by coating the solution mixed in an ultrasonicator for 30 min. These images show that WO_3 particles attached well to the MWCNTs. In addition, the high-resolution TEM (HRTEM) images of MWCNTs reveal stacked wavy nanotube walls, indicating an imperfect distorted layered structure (Fig. 3c). The respective fast Fourier transform (FFT) plots, revealing wide blurry dots (Fig. 3d), are characteristic of MWCNTs with numerous defects [30]. For MWCNTs, defects can be divided into two groups, namely sp^2 and non-sp^2 defects [30,31]. The sp^2 defects reflect the existence of pentagons, heptagons, and/or octagons in the MWCNT lattices. Bond-rotation-based defects, such as 5-7-7-5 defects and heptagon-pentagon pairs, also belong to the category of sp^2 defects. They correspond to the distorted MWCNT lattices in Fig. 3c. Moreover, these defects can cause nanotubes to bend into different shapes and are always associated with the curved and/or entangled morphologies of MWCNTs. The non-sp^2 defects in MWCNTs correspond to reactive carbon atoms, such as vacancies, interstitial atoms, and edges in open nanotubes. We posit that many non-sp^2 defects in our MWCNTs caused WO_3 particles to attach firmly to the MWCNT surfaces. The HRTEM images of WO_3 particles suggest good crystallinity, as exhibited by the FFT images of clear and strong dots (Fig. 3e and f). The planar distance of 0.263 nm is ascribed to the (202) plane of the monoclinic WO_3 structure, as confirmed by XRD measurements.

Fig. 4a shows the XRD spectra of MWCNTs (yellow, also magnified in the inset), WO_3 (black), and WO_3/MWCNT composites (cyan). The strong and sharp diffraction peaks suggest the high crystallinity of WO_3, and these observations agree well with the TEM and FFT results in Fig. 3e and f. The diffraction peaks in Fig. 4a can be attributed to the monoclinic WO_3 crystalline structure (JCPDS No. 43–1035) [32], and no other impurity-related peaks are detected for this resolution. The XRD spectrum of MWCNTs, shown in the inset, exhibits the characteristic diffraction peak of (002) at 25.6°, which is in a good agreement with previous findings [33,34]. A small peak at 42.5° is ascribed to the (100) lattice plane, while its broadness illustrates the disorder associated with the MWCNTs. The MWCNTs peak was not observed for the WO_3/MWCNT composites, mainly owing to the small amount of MWCNTs.

Fig. 4b shows the Raman spectra of WO_3, WO_3/MWCNT composite, and MWCNTs. The Raman spectrum of MWCNTs shows the so-called D-band and G-band peaks at 1350 cm^{-1} and 1576 cm^{-1}, respectively. The G-band peak is attributed to the C–C vibration with the sp^2 hybridized orbital in graphene structures, whereas the D-band peak is attributed to disordered sp^2 and non-sp^2 carbon defects in graphitic sheets [30]. The D-band peak intensity, compared with that of the G-band peak, is a measure of the crystallinity of MWCNTs. The weak peak at 1638 cm^{-1} is caused by intercalated graphite compounds and strain in the C–C bond [30]. Fig. 4b also shows the Raman spectrum of WO_3, with four peaks at 261, 321, 704, and 803 cm^{-1}. The former two peaks are attributed to the W–O–W bending vibration modes, while the latter two peaks are attributed to the W–O–W stretching vibration mode in WO_3 [35]. Fig. 4c shows the ratio of the D-band to G-band intensities (I_D/I_G) for the WO_3/MWCNT composite, which is higher than that for pristine MWCNTs, indicating that more defects were generated in the MWCNTs after mixing [34,36,37]. In addition to the breaking up of the MWCNTs during the mixing, the attachment of the WO_3 particles to the surfaces of the MWCNTs could increase the I_D/I_G ratio.

3.2. Electrical properties

For understanding and discussing the electrical and gas detection characteristics of the fabricated WO_3/MWCNT composites, the band parameters of MWCNTs and WO_3 were determined by UPS measurements (Fig. 5a and b). The contact properties of the WO_3/MWCNT composites were further examined by XPS, and the results are summarized in Fig. 5c. The work functions determined for MWCNTs and WO_3 by the UPS measurements were 4.66 eV and 4.45 eV, respectively. These values are slightly smaller than those that were previously determined using other methods [38–41], and the chirality and diameter may alter the properties of MWCNTs [42]. The MWCNTs in this study exhibited p-type doping behavior, but the small bandgap energy [43] led to a very low resistance of a metallic conductivity (~43 Ω as will be shown below). This suggests that a p^+n MWCNT/WO_3 high-low heterojunction can be formed, as illustrated in Fig. 5d, where the depletion layer is effectively formed in WO_3 with a built-in potential (Φ_b) of 0.21 V. This heterojunction property was further confirmed by the XPS measurements in Fig. 5c. While XPS survey spectrum confirmed neither contaminants nor Ni doping in WO_3 (Fig. S3), the high-resolution XPS spectra of W 4f for the pristine WO_3 revealed the binding energies of 35.47 eV and 37.66 eV, which were respectively ascribed to the W $4f_{7/2}$

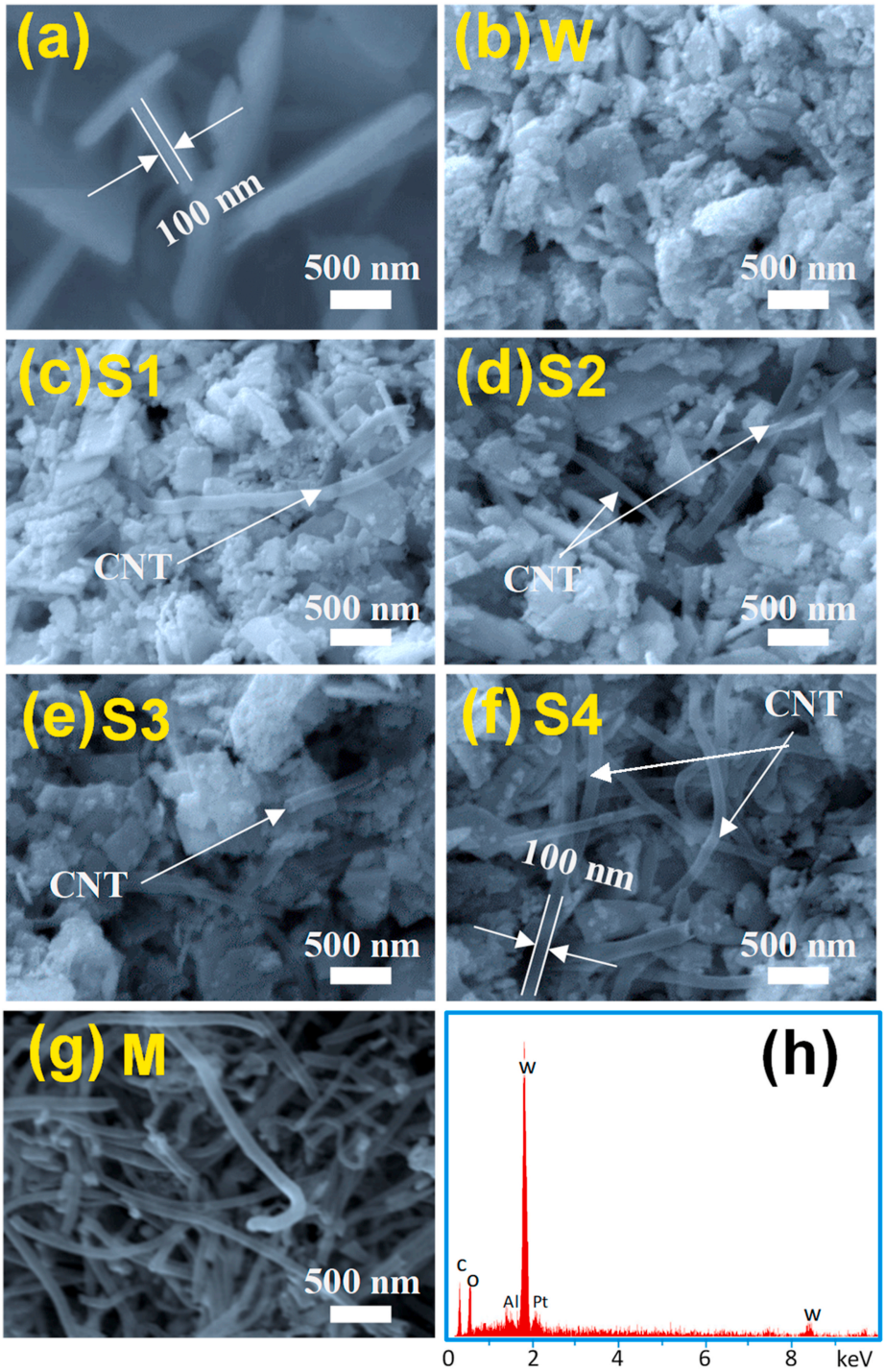

Fig. 2. SEM images of (a) as-synthesized WO_3 flakes, (b) WO_3 sensor (W), (c–f) WO_3/MWCNT sensors with different weight percentages of MWCNTs, that is S1 (0.25 wt%), S2 (0.5 wt%), S3 (1 wt%), and S4 (5 wt%), respectively, and (g) MWCNT sensor (M). (h) EDS spectrum of the WO_3/MWCNT sensor S2.

and W $4f_{5/2}$ orbitals of the W^{6+} state in WO_3 [44]. However, the binding energies slightly increased, to 35.71 eV and 37.9 eV, for the WO_3/MWCNT composites. The upward shift can be explained by the transfer of electrons from WO_3 to MWCNTs, and positive ions that are left behind in WO_3 retard photoelectrons causing the peaks to appear at higher binding energies [44]. This result supports the band diagram for the WO_3/MWCNT heterojunction shown in Fig. 5d.

Fig. 6a shows the transient response curves measured of the sensor structures, in 5 ppm NO_2 at 150 °C. First, note that the base resistance (R_o), measured in dry air, decreases with increasing the MWCNT content. The pure WO_3 (W) structure exhibits R_o of ~2×10^8 Ω, while the pure MWCNT (M) structure exhibits the resistance of ~43.2 Ω; the conductivity difference is more than six orders of magnitude, assuming the same thickness. Second, the sensing response curves reveal that WO_3 is an n-type semiconductor while MWCNT is a p-type semiconductor, as shown in Fig. 6a and b. The conductivity σ is the product of the carrier concentration and mobility, as captured by the relationship $\sigma = e\mu_n n + e\mu_p p$ (where μ is the mobility, and n and p are the electron and hole concentrations, respectively). Taking the WO_3 electron mobility as $10^{-1} - 10^1$ cm^2/V-s [45,46] and taking the CNT hole mobility as $10^2 - 10^4$ cm^2/V-s [47–49], as given in the literature, the hole concentration in MWCNTs is on the order of 10^2–10^6 times the

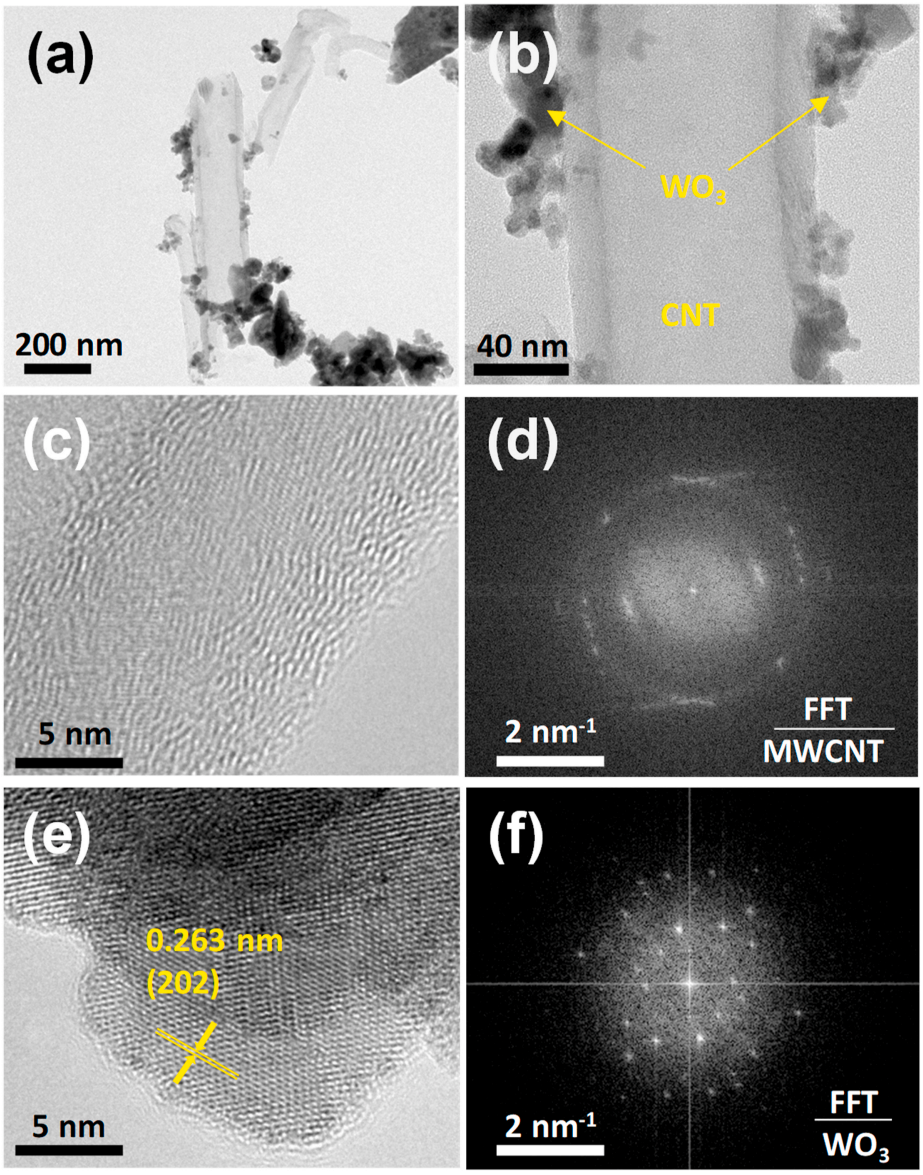

Fig. 3. (a, b) TEM images at different magnifications, showing that WO_3 particles firmly attach to MWCNTs. The respective HRTEM and FFT images of (c, d) MWCNTs and (e, f) WO_3.

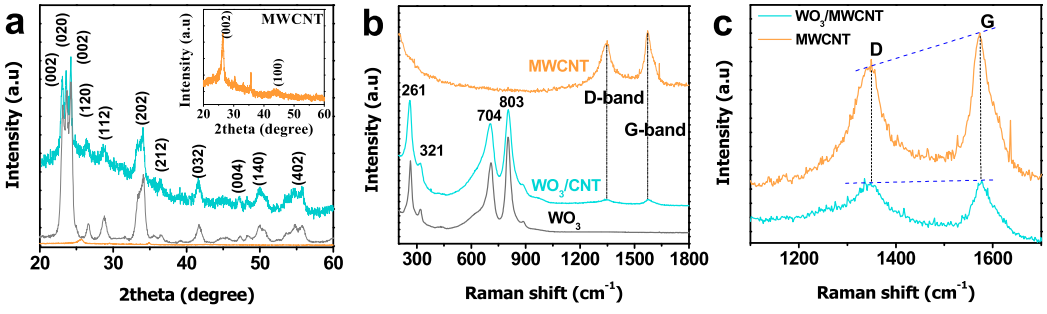

Fig. 4. (a) XRD of MWCNTs (orange line), WO_3 (gray line), and WO_3/MWCNTs (cyan line). The inset shows the amplified view of the XRD spectrum of the MWCNTs. (b) Raman spectra for the same. (c) A magnification of (b) to compare the G- and D-bands of the MWCNTs. (For interpretation of the references to color in this figure legend, the reader is referred to the Web version of this article.)

electron concentration in WO_3. However, we may consider MWCNTs as a metallic conductor, owing to a very high concentration of carriers in MWCNTs, compared with WO_3. Thus, MWCNTs provide the main conduction mechanism in MWCNT/WO_3 composites.

We also considered the electrical properties of the structures at 150 °C in dry air. The W sample is a thin film of agglomerated WO_3 nanoparticles, as shown schematically in Fig. 7a:W. For uniform particle size and film thickness, this thin film may be approximated as a one-dimensional collection of WO_3 nanoparticles connected in series, as shown in Fig. 7b:W, where not only the structural network but also the number of NO_2 molecules adsorbed is shown, according to the modulated charge. The equivalent circuit for this pure WO_3 thin film is shown by Fig. 7c:W. Similar schematics, for the n-type S1–S3 composites, p-type S4 composite, and pure MWCNT sensor, are shown in Fig. 7.

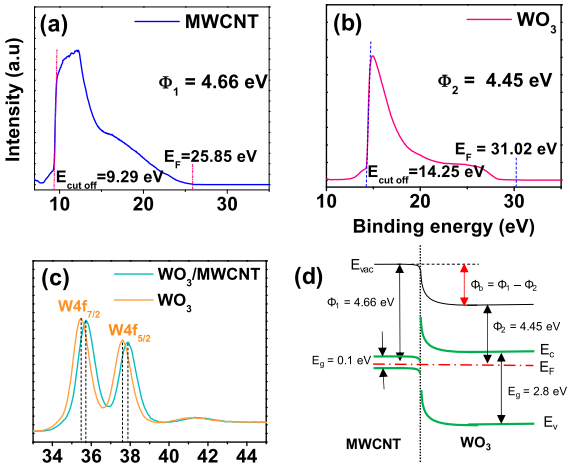

Fig. 5. UPS profiles of (a) MWCNTs and (b) WO_3. (c) High-resolution XPS spectra of the W $4f_{7/2}$ and W $4f_{5/2}$ orbitals of W^{6+}, with an upward shift for MWCNTs, owing to the formation of the Schottky junction. (d) The energy band diagram of WO_3/MWCNT contacts shows the electron transfer trend in the initial contact state and the formation of a potential barrier Φ_b (0.21 eV) in the equilibrium state (not scaled).

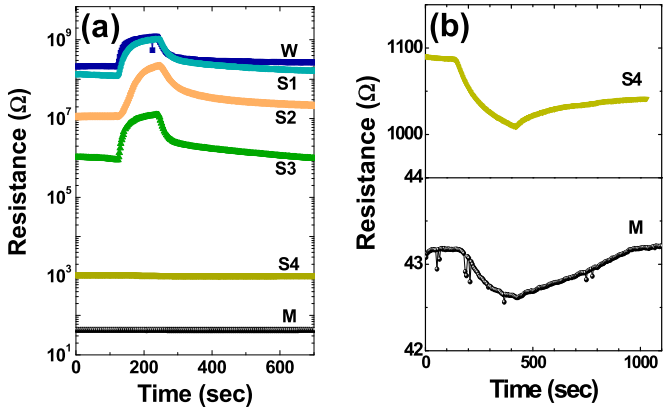

Fig. 6. (a) Base resistances and transient response curves of the composite sensor structures, in 5 ppm NO_2 at 150 °C. (b) Magnified views for the S4 and M sensors.

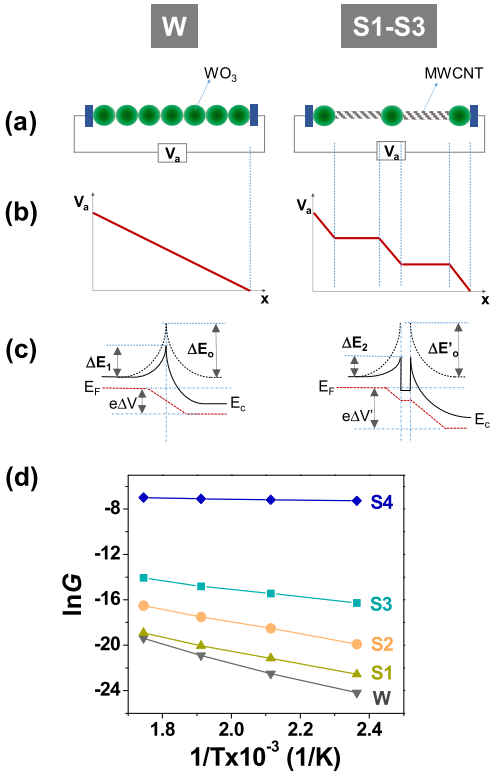

Fig. 8. (a) Schematic of the sensor structures in series connections of WO_3 particles (left) and WO_3/MWCNT (right). (b) Potential drop in the structures under external biasing. (c) Conduction band edge profiles for WO_3/WO_3 and WO_3/MWCNT/WO_3 junctions in the thermal equilibrium (dashed curve) and under biasing (solid curve). Potential drops at the junctions different between the structures are shown. (d) Conductance vs. 1/T plots, exhibiting barrier energies for transport variation in the structures.

When an external bias of V_a is applied on the electrodes of the W structure (Fig. 8a:W), in the macroscopic view, the nanoparticles act as an equipotential body, as shown in Fig. 8b:W. On the other hand, the potential drop for one particle is $\Delta V = V_a/n$ if n particles are connected in series. In the microscopic view of the particles, the potential drop mainly occurs through the carrier-depleted junction of high resistivity. This is the generally accepted back-to-back Schottky contact formed at the particle-to-particle interface, which originates from the surface states including oxygen adsorption in the air. The conduction band edge

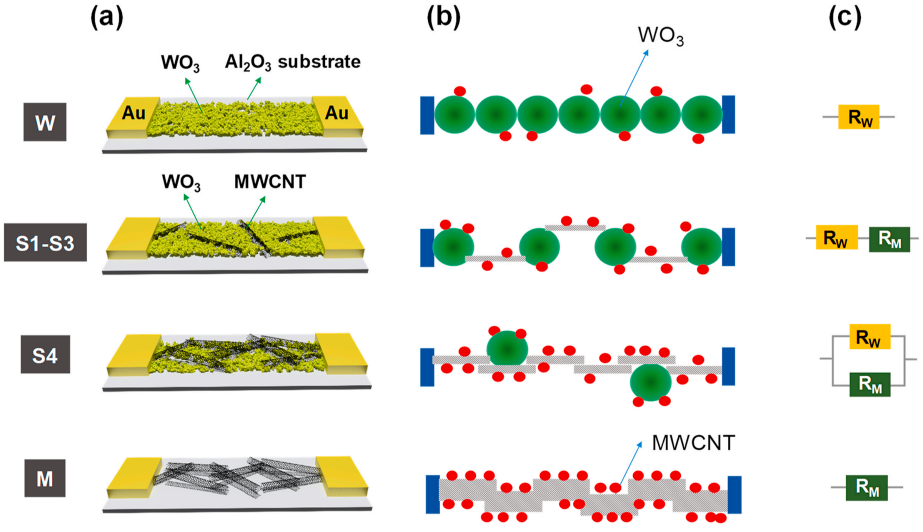

Fig. 7. (a) Schematics of the sensor structures (WO_3, WO_3/MWCNT, and MWCNT), (b) corresponding schematics for the adsorption of NO_2 molecules (red dots), the number of which increases with increasing the MWCNT content in the composites and (c) equivalent circuits. (For interpretation of the references to color in this figure legend, the reader is referred to the Web version of this article.)

Table 1
The BET measurement results for the composites with different MWCNT contents. The results were converted to per volume units (m^2/cm^3), using the molecular weights of 231.84 and 12.01 for WO_3 and MWCNTs, respectively. R(meas) values are from Fig. 6a and R(parallel calc) values were calculated assuming the current transport along the parallel circuit of MWCNT and WO_3 resistors.

	W	S1	S2	S3	S4	M
MWCNT(wt%; vol%)	0	0.25; 4.6	0.5; 8.8	1.0; 16.3	5.0; 50.4	100
BET(m^2/g)	19.4	23.9	26.0	29.3	40.8	96.5
BET(m^2/cm^3)	139	140	140	141	150	218
R(meas)	2.1×10^8	1.2×10^8	1.1×10^8	9.7×10^7	1.1×10^3	43
R(parallel calc)	2.1×10^8	5.5×10^3	2.7×10^3	1.4×10^3	3.0×10^2	43

profile under bias is shown in Fig. 8c:W, which signifies the potential drop ΔV that is effectively applied through the electron depleted Schottky junction. The conduction band edge profile should be compared with that at the contact in the thermal equilibrium (dashed curve) showing the barrier height of ΔE_o. The external bias of ΔV lowers the barrier energy to ΔE_1, generating an electron flux over the barrier, given by

$$J \propto \exp(-\Delta E_1/kT) \quad (5)$$

This electron flux determines the resistance R_W, as shown in the equivalent circuit diagram in Fig. 7c:W.

Meanwhile, in the n-type WO_3/MWCNT composites of S1–S3 fabricated for higher MWCNT content, the MWCNT short wires serve as a preferential path for the flow of electrons. However, since the MWCNT content is not sufficiently high for forming continuous networks in these structures, the gaps between the MWCNT wires are bridged by WO_3 particles. These structures are schematically shown in Fig. 7a:S1–S3 and **7b:S1–S3**, depicting the alternating arrangement of MWCNTs and WO_3 particles in these structures. The equivalent electrical circuit is an in series connection of R_W and R_M (Fig. 7c:S1–S3). Note that the resistance of these structures is mainly determined by the volume ratio of WO_3 and MWCNTs in the composites, but the determining factor is high-resistivity R_W.

The S1–S3 structures with an alternative arrangement of MWCNTs and WO_3 are shown again in Fig. 8a:S1–S3. Accordingly, the potential drop occurs effectively only in WO_3, as shown in Fig. 8b:S1–S3, where the bias potential is applied effectively to WO_3 particles. Thus, the potential that is applied to an individual WO_3 particle is higher than that in Fig. 8a:W. The potential drop over an individual WO_3 particle increases with increasing MWCNT content in the composites, decreasing the resistance of the sample. This trend is clearly seen in Fig. 6a. The alternating WO_3/MWCNT contacts can be approximated by short-circuited back-to-back WO_3/WO_3 Schottky contacts, as marked in Fig. 8c:S1–S3 by the dashed curve in the thermal equilibrium.

Compared with the W sample, the higher potential applied to WO_3 particles ($\Delta V' > \Delta V$) lowers the barrier energy for electron transfer ($\Delta E_2 < \Delta E_1$), as shown in Fig. 8c:S1–S3, resulting in a higher current flow, that is, a lower resistance in the structures. The barrier energies measured for the structures are summarized in Fig. 8d, in which the conductance of the samples was measured at different temperatures (Fig. S4, Supporting Information). The barrier energy $\Delta E_1 = 0.57$ eV measured for W decreased to $\Delta E_2 = 0.45$ eV for S2 when MWCNTs were added, which explains the difference observed in Fig. 8c. The continuously decreasing resistance from W to S1 to S3 (Fig. 6a) coincides with the continuously decreasing slopes in Fig. 8d. The S1–S3 composites are denoted by the same equivalent circuit as in Fig. 7c:S1–S3, namely a series connection of resistances $R_W + R_M$, but with different component values. As the MWCNT content in the composites increased, R_W decreased as R_M increased. However, the reduction in ΔR_W was greater than the increase in ΔR_M; thus, the overall resistance decreased. The decrease in R_W with increasing MWCNT volume ratio in the composites is explained in Fig. 8b, which shows a higher potential drop at individual WO_3 particles for smaller WO_3 volume ratios in the composites, which in turn results in a smaller ΔE_2 in Fig. 8c. Therefore, the overall current in the S1–S3 structures is determined by the electron transport through the n-type WO_3 particles short-circuited via the metallic MWCNTs, and thus, the structures exhibit the n-type behavior.

The steep decrease in resistance for S4 (compared with the W and S1–S3 samples) originated from high-conduction paths formed by the percolation of MWCNTs in the composite film. When MWCNT wires formed a continuously connected network in high-MWCNT-content composites (Fig. 7a:S4); the equivalent circuit is a parallel circuit of R_M and R_W (Fig. 7c:S4). Most of the current flows through the MWCNTs because $R_M \ll R_W$, which is also supported by the observations of the dramatically shallower slope for S4 (0.03 eV), as shown in Fig. 8d. To present a complete picture, the schematic and the equivalent circuit for the M sample for the percolation structure of pure MWCNTs is shown in Fig. 7:M.

The BET measurements (Fig. S5), summarized in Table 1, also support the conclusions of the above discussion. To correlate the BET results with the sample conductance results, the weight % values for the MWCNTs in the composites were converted to volume % using the molecular weights of 231.84 and 12.01 for WO_3 and MWCNTs, respectively. The conversion results are also listed in Table 1. Owing to the strong difference between the two molecular weights, the 5 wt% MWCNTs were converted to ~50 vol% MWCNTs for the S4 sample. The BET values measured per weight were accordingly converted to those per volume, because the current density was measured per the cross-sectional area of the current path. Note also that the measured total surface area for MWCNTs was ~1.5 (=218/139) times greater than that for WO_3. The ratio also indicates that WO_3 particles are ~1.5 times larger than MWCNTs.

Based on the basic characteristics of the studied nanoparticles, an interesting observation is that the BET per volume barely changed until the MWCNT content increased to 16.3 vol% (S1–S3). The results indicate that the surface area of the composites did not strongly change following the mixing with MWCNTs at relatively low concentrations. Even with 1:1 vol ratio for S4, the surface area increased owing to the MWCNTs not as much as the incorporated volume in the composite. Therefore, the surface area for interaction with gases did not strongly vary across the different composite structures. This may be explained by the similar BET values per volume for MWCNTs and WO_3. The BET measurements were further correlated to the structures' resistance. The R(meas) values in the table list the base resistance values of the structures, measured at 150 °C in dry air (Fig. 6a). The R(parallel calc) values were calculated assuming that both the electrical conduction paths of MWCNTs and WO_3 nanoparticles run in parallel in the structures. This assumption is rather arbitrary, because MWCNTs in smaller-content structures (S1 to S3) are not likely to form continuous networks. However, our calculations showed that the resistance of the composite must decrease to ~10^3 Ω, even if a path is formed that consists of thin MWCNTs. The fact that the actually measured values (~10^8 Ω) were very much different from the calculation results suggests that no such continuous MWCNT paths were actually formed in the composites S1–S3. This analysis supports the interpretation of an in series connection of WO_3 and MWCNTs in the samples S1–S3. On the other hand, a strong reduction in the value of R(meas) (approaching R

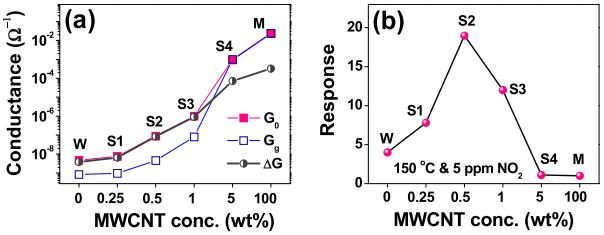

Fig. 9. (a) G_o, G_g, and ΔG values extracted from Fig. 6a. (b) Dependence of the sensor response on the MWCNT content, for composite sensor structures.

(parallel calc)) for S4 suggests MWCNT-mediated percolation and establishment of a parallel path of WO_3 and MWCNTs in this composite. This explanation is consistent with the measured very small barrier energy, ΔE = 0.03 eV, for S4. Therefore, we can safely confirm the electrical structures for the samples that were postulated in Fig. 7.

3.3. NO_2 adsorption properties

The response curves in Fig. 6a were converted and are shown in Fig. 9a, where the baseline conductance ($G_o = 1/R_o$), the conductance under exposure to 5 ppm NO_2 ($G_g = 1/R_g$), and their difference $\Delta G = |G_o - G_g|$ are plotted. The conversion from resistance to conductance is useful for discussing the concentration of carriers in the structures of interest. Because the sensor's G value is proportional to the concentration of free carriers in the corresponding structure, ΔG represents the charge modulation in the transducer owing to the supply of electrons to the receptor surface for adsorption of NO_2 molecules. There are two remarkable results to be noted in Fig. 9a in relation to the sensing mechanism in composite sensors. First, ΔG monotonically increases with the MWCNTs content, meaning that the number of adsorbed NO_2 molecules continuously increases with increasing the number of MWCNTs in the composite. The ΔG value for a structure with MWCNTs was almost 10^5 times that for the structure with WO_3 (Fig. 9a). Second, the ratios of the charge modulation to the initial charge ($\Delta G/G_o$) were very different for the n-type and p-type sensors: $\Delta G/G_o \approx 1$ and $\Delta G \approx G_o \gg G_g$ for W and S1–S3 n-type sensors, while $\Delta G/G_o \approx 0$ and $\Delta G \ll G_o \approx G_g$ for S4 and M p-type sensors. The resultant sensing response levels are summarized in Fig. 9b. The maximal response was observed for the n-type composite sensor S2. The lower and higher MWCNT contents in the composites degraded the sensing performance. In particular, p-type sensors with excess MWCNTs exhibited negligible responses.

The n-type composites (W and S1–S3) exhibited strong charge modulation upon NO_2 adsorption, with most of the electrons in the sensors transported to the surface ($\Delta G \approx G_o$). For example, the pure WO_3 thin film exhibited G_o = 4.8 nS and G_g = 0.8 nS, resulting in ΔG = 4.0 nS, which corresponded to $\Delta G/G_o \approx 0.83$ or to ~83% of the electrons in the film being at the WO_3 surface for NO_2 ionosorption. The composite S2 that exhibited the maximal response (Fig. 9b) had G_o = 89 nS, G_g = 4.5 nS, and ΔG = 84 nS, corresponding to ~94% of the electrons in the sample being at the surface. Thus, the number of adsorbed NO_2 molecules for S2 was ~21 times higher than that for the pure WO_3. The two structures had nearly the same specific surface areas, as shown in Table 1. The results for the number of adsorbed NO_2 molecules for the two structures are shown in Fig. 7b:W and 7b:S1–S3 with red dots, and the relation of these results to the sensors' response characteristics can be explained as follows.

The giga-ohm range resistance of WO_3 can be attributed to the small sizes of WO_3 particles, which are almost depleted of electrons. The electrons for NO_2 ionosorption must be supplied from the interior of the WO_3 particles, but the number of electrons is not sufficient for accommodating all of the surface adsorption sites; thus, only some adsorption sites can be occupied by NO_2. However, in the WO_3/MWCNT composites, MWCNTs serve as a reservoir of electrons that are scattered throughout the composites, and supply electrons to impinging NO_2 molecules for ionosorption on WO_3 particles and MWCNTs. Considering the volume of MWCNTs, which was typically below 10% for the studied composites, this explains the observed 21-fold increase in the number of electrons supplied for adsorption on WO_3 receptors. We also showed that, with hematite/single-wall CNT composites, high-conductance single-wall CNTs supply holes to oxide receptors, increasing the adsorption of ammonia gas molecules [22]. Therefore, MWCNTs distributed in oxide nanoparticles agglomerate can play the role of a reservoir that supplies electrons for NO_2 adsorption on the oxide nanoparticles' surfaces.

The charges transported between WO_3 and MWCNTs in a minute, as shown by the response curves in Fig. 6a. Further increasing the MWCNT content of S3 increased the electron supply (G_o = 1.1 μS) and the number of NO_2 adsorptions (ΔG = 1.0 μS) by more than 10-fold for S2, but the response decreased because a relatively large number of electrons remained in the MWCNTs (G_g = 80 nS), which slightly decreased the response G_o/G_g. In conclusion, in the n-type WO_3/MWCNT composite sensors, both WO_3 and MWCNTs serve as receptors for NO_2, but the required electrons for ionosorption are mostly supplied by the metallic MWCNTs scattered throughout the film. The p-type but metallic nature of MWCNT can be explained in terms of the small bandgap energy. The n-type sensing behavior of the sensor films can be explained by a continuous network of n-WO_3 nanoparticles, while p-MWCNTs form a discontinuous network. Response enhancement of the composites was driven by increasing ΔG, through the expression $S = G_o/(G_o - \Delta G)$.

When the MWCNT content was further increased, a percolating, or continuous, network of MWCNTs was formed. This condition was realized with the composite S4 and the network of pure MWCNTs representing p-type high-conductance transduction (G_o = 0.99 mS). A continuous network of WO_3 could also form in parallel, as shown in Fig. 7c:S4, but its contribution to the current flow would be negligibly small. The number of adsorbed NO_2 molecules significantly increased with increasing the number of MWCNTs with high specific surface area (ΔG = 74 μS; Fig. 7b:S4), but ΔG was very small compared with G_o, exhibiting a very small response approaching ~1, owing to $S = (G_o + \Delta G)/G_o$ (S4 in Figs. 6b and 9b). The ultimate extreme case was provided by the pure MWCNT sensor, which exhibited the highest ΔG and G_o, but again exhibited a poor response. Therefore, the observed relatively poor response of CNT-based sensors could be attributed to the excess of CNTs in the films [18,19].

The discussion of the sensing characteristics of the composites is based on the transconductance modulation that is caused by the depletion depth modulation on the receptors' surfaces. This model has been repeatedly confirmed by these researchers for various nanostructured gas sensors [7,50–52]. The model claims that the maximal response of a nanostructured one-component sensor is obtained when the sensor's dimensions approach the depletion depth scale; a further size reduction will negatively affect the sensor's response. Therefore, the ultimate gas sensing performance is already determined by the sensor's dimensions and by the doping level, for a given gas-material system. However, composites can overcome the limitation of one-component sensor structures. As we have discussed so far, the receptor and transducer roles can be separated in composites. Given a composite, the optimal ratio of its constituents emerges as a synergetic effect, and can be determined by considering a range of ratios. In addition, the back-to-back Schottky barrier model cannot consistently explain the results observed for a series of nanostructured composite sensors.

The NO_2 sensing performances of the studied sensors were measured at different temperatures (Fig. S6, Supporting Information), and the response levels are summarized in Fig. S7a. As the temperature increases, the carrier concentrations in WO_3 and MWCNTs increase, and the depletion depth decreases, in accord with the semiconductor junction theory. The peak response at 200 °C for the W sensor is the intrinsic response of WO_3 toward the adsorption of NO_2, and the peak

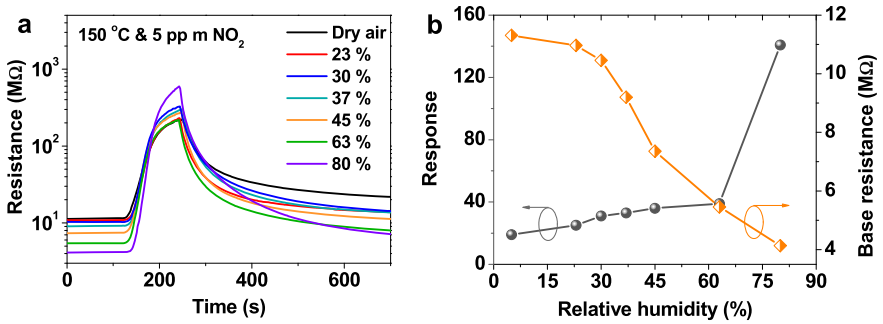

Fig. 10. (a) The sensing curves of S2 sensor measured at 150 °C for 5 ppm NO_2 with varying RH. (b) The base resistances and responses plotted from (a).

temperature decrease in the n-type composites is the MWCNT effect. A reduction in the optimal sensing temperature with CNT mixing has been often observed [14]. While the response of S2 at 100 °C increased, the response-recovery kinetics were very slow and highly irreversible for practical use (Fig. S6f). As the temperature increased to 300 °C, a strong increase in the concentration of carriers in the transducer lowered the response, for all of the studied composite structures. Fig. S7b shows the gas concentration dependence of the W and S2 sensor responses. The S2 composite sensor also exhibited good selectivity, high repeatability, and short response/recovery times (87 s /300 s), as shown in Fig. S7c, **7d**, and 7**e** which suggests that commercial NO_2 sensors can be developed by utilizing these insights.

The effect of humidity examined at the operation temperature 150 °C with the S2 sensor is shown in Fig. 10. The resistance of the sensor decreased continuously with increasing of relative humidity (RH). This change can be explained by electron donation from water molecules to the sensor, as was also observed with other oxide sensors fabricated in this lab [22,27,28,53]. Since the humidity effect is not negligible, a parallel use of humidity sensor is required for humidity calibration [27]. The sensing performance of several metal oxide/carbon material-based nanosensors are compared in Table 2 [15,16,18,19,54–59]. Our sensor showed similar or better performance among different types of oxide composites, and in particular, exhibited superior response/recovery kinetics to other sensors.

4. Conclusions

A series of WO_3/MWCNT composite sensors with different WO_3/MWCNT ratios were fabricated, and their electrical and gas sensing properties were scrutinized for determining their correlation with the sensors' morphologies. The cornerstone assumption of this study was conduction-mediated gas sensor; that is, the difference between the conductance values before and after the exposure to gaseous NO_2 resulted from its ionosorption, and involved charge exchange. The specific surface areas of the WO_3 and MWCNT components, measured using the BET method, did not differ significantly. However, the densities of NO_2 adsorption (more precisely the modulated charges) on the components' surfaces were very different for MWCNTs and WO_3. The WO_3 nanoparticles were relatively lightly doped and almost depleted of electrons; consequently, the electrons supplied for NO_2 adsorption were not sufficient for occupying the allowed adsorption sites on the surfaces. The other extreme was observed for metallic MWCNTs, which can supply a sufficient number of electrons for fully occupying the NO_2 adsorption sites on the surfaces, but the supplied electrons were only a small fraction of the electrons in MWCNTs. Owing to different reasons, both pure WO_3 and MWCNT sensors exhibited poor NO_2 sensing performance. However, composites of WO_3 and MWCNTs demonstrated much better sensing performance. The optimal combination was obtained for the composite in which the number of adsorption sites on the receptors' surfaces (WO_3 and MWCNTs) was equal to the number of electrons in the transducer (approximately to that of MWCNTs). This condition was satisfied for sample S2 when: i) WO_3 particles were connected in series with MWCNTs and ii) the carrier transport across the interface was rather free. Therefore, mixtures of low-doped oxides with reservoirs of carriers can exhibit synergetic effects yielding conduction-type gas sensors by: i) maximizing the number of adsorption sites and adsorption gas molecules and ii) providing marginally sufficient numbers of carriers for ionosorption. We further showed that the Schottky barrier model frequently employed in sensors for explaining the responses of thick-film sensors of agglomerated nanoparticles cannot be used for explaining the operation of nanocomposite sensor structures.

Declaration of competing interest

The authors declare that they have no known competing financial interests or personal relationships that could have appeared to influence the work reported in this paper.

Table 2
Performance of several metal oxide/carbon material-based NO_2 gas sensors.

Materials	[NO2]/ppm	T/oC	Response (Rg/Ra)	tres/trec	Reference
rGO-loaded SnO_2	5	200	100	−/−	[59]
CuO–ZnO/rGO	40	RT	[a]62.9 %	−/−	[58]
CNTs/SnO_2	50 ppb	RT	[a]59 %	15 min /3 min	[57]
rGO/ZnO composite	5	250	[a]700 %	−/−	[56]
ZnO/SWCNT composite	50	150	5	70 s /100 s	[15]
SnO_2/Graphene composite	5	150	72.6	250 s /500 s	[55]
WO_3/rGO composite	10	RT	[a]769 %	9 min /18 min	[54]
WO_3/MWCNT composite	2.5	200	~5	200 s /400 s	[19]
WO_3/MWCNT composite	5	150	1.05	5 min/-	[18]
WO_3/CNT composite	5	200	3.8	−/−	[16]
WO_3/MWCNT composite	5	150	18	87 s /300 s	This study

RT: room temperature.
[a] Response = (Rg-Ra)/Ra * 100 %.

Acknowledgments

This work was supported by the National Research Lab program (2018R1A2A1A 05023126) of the National Research Foundation of Korea.

Appendix A. Supplementary data

Supplementary data to this article can be found online at https://doi.org/10.1016/j.ceramint.2020.08.097.

References

[1] X. Liang, W. Liu, Y. Cheng, J. Lv, S. Dai, D. Tang, B. Zhang, G. Ji, Review: recent process in the design of carbon-based nanostructures with optimized electromagnetic properties, J. Alloys Compd. 749 (2018) 887–899.
[2] O.S. Okwundu, E.U. Aniekwe, C.E. Nwanno, Unlimited potentials of carbon: different structures and uses (a Review), J. Inst. Eng. 24 (2018) 145–171.
[3] H.-i. Kim, M. Wang, S.K. Lee, J. Kang, J.-D. Nam, L. Ci, J. Suhr, Tensile properties of millimeter-long multi-walled carbon nanotubes, Sci. Rep. 7 (2017) 1–7.
[4] A. Peigney, C. Laurent, E. Flahaut, R. Bacsa, A. Rousset, Specific surface area of carbon nanotubes and bundles of carbon nanotubes, Carbon 39 (2001) 507–514.
[5] T. Shimizu, H. Abe, A. Ando, Y. Nakayama, H. Tokumoto, Electrical conductivity measurements of a multi-walled carbon nanotube, Surf. Interface Anal.: An International Journal devoted to the development and application of techniques for the analysis of surfaces, interfaces and thin films 37 (2005) 204–207.
[6] C.M. Hussain, C. Saridara, S. Mitra, Self-assembly of carbon nanotubes via ethanol chemical vapor deposition for the synthesis of gas chromatography columns, Anal. Chem. 82 (2010) 5184–5188.
[7] S. Moon, N.M. Vuong, D. Lee, D. Kim, H. Lee, D. Kim, S.-K. Hong, S.-G. Yoon, Co3O4–SWCNT composites for H2S gas sensor application, Sensor. Actuator. B Chem. 222 (2016) 166–172.
[8] G.D. Nessim, Properties, synthesis, and growth mechanisms of carbon nanotubes with special focus on thermal chemical vapor deposition, Nanoscale 2 (2010) 1306–1323.
[9] A. Yahyazadeh, B. Khoshandam, Carbon nanotube synthesis via the catalytic chemical vapor deposition of methane in the presence of iron, molybdenum, and iron–molybdenum alloy thin layer catalysts, Results Phys. 7 (2017) 3826–3837.
[10] X. Dong, M. Al Awak, P. Wang, Y.-P. Sun, L. Yang, Carbon dot incorporated multi-walled carbon nanotube coated filters for bacterial removal and inactivation, RSC Adv. 8 (2018) 8292–8301.
[11] L.-Q. Rong, C. Yang, Q.-Y. Qian, X.-H. Xia, Study of the nonenzymatic glucose sensor based on highly dispersed Pt nanoparticles supported on carbon nanotubes, Talanta 72 (2007) 819–824.
[12] X. Ye, J. Ma, Y.-S. Hu, H. Wei, F. Ye, MWCNT porous microspheres with an efficient 3D conductive network for high performance lithium–sulfur batteries, J. Mater. Chem. 4 (2016) 775–780.
[13] D.-J. Yun, K. Hong, S.H. Kim, W.-M. Yun, J.-y. Jang, W.-S. Kwon, C.-E. Park, S.-W. Rhee, Multiwall carbon nanotube and poly (3, 4-ethylenedioxythiophene): polystyrene sulfonate (PEDOT: PSS) composite films for transistor and inverter devices, ACS Appl. Mater. Interfaces 3 (2011) 43–49.
[14] T. Ueda, M. Bhuiyan, H. Norimatsu, S. Katsuki, T. Ikegami, F. Mitsugi, Development of carbon nanotube-based gas sensors for NOx gas detection working at low temperature, Phys. E Low-dimens. Syst. Nanostruct. 40 (2008) 2272–2277.
[15] S. Barthwal, B. Singh, N.B. Singh, ZnO-SWCNT Nanocomposite as NO2 gas sensor, Mater. Today: Proc. 5 (2018) 15439–15444.
[16] T. Hashishin, J. Tamaki, Conductivity-type sensor based on CNT-composite for NO2 detection, J. Nanomater. (2008) 2008.
[17] H. Liu, W. Zhang, H. Yu, L. Gao, Z. Song, S. Xu, M. Li, Y. Wang, H. Song, J. Tang, Solution-processed gas sensors employing SnO2 quantum dot/MWCNT nanocomposites, ACS Appl. Mater. Interfaces 8 (2016) 840–846.
[18] C. Bittencourt, A. Felten, E. Espinosa, R. Ionescu, E. Llobet, X. Correig, J.-J. Pireaux, WO3 films modified with functionalised multi-wall carbon nanotubes: morphological, compositional and gas response studies, Sensor. Actuator. B Chem. 115 (2006) 33–41.
[19] N. Van Duy, N.D. Hoa, N.T. Dat, D.T.T. Le, N. Van Hieu, Ammonia-gas-sensing characteristics of WO3/carbon nanotubes nanocomposites: effect of nanotube content and sensing mechanism, Sci. Adv. Mater. 8 (2016) 524–533.
[20] F. Özütok, I.K. Er, S. Acar, S. Demiri, Enhancing the Co gas sensing properties of ZnO thin films with the decoration of MWCNTs, J. Mater. Sci. Mater. Electron. 30 (2019) 259–265.
[21] Q.T.M. Nguyet, N. Van Duy, C. Manh Hung, N.D. Hoa, N. Van Hieu, Ultrasensitive NO2 gas sensors using hybrid heterojunctions of multi-walled carbon nanotubes and on-chip grown SnO2 nanowires, Appl. Phys. Lett. 112 (2018) 153110.
[22] N.M. Hieu, C.V. Phuoc, T.T. Hien, N.D. Chinh, N.D. Quang, C. Kim, J.-R. Jeong, D. Kim, A separated receptor/transducer scheme as strategy to enhance the gas sensing performance using hematite–carbon nanotube composite, Sensors 19 (2019) 3915.
[23] S. Li, P. Lin, L. Zhao, C. Wang, D. Liu, F. Liu, P. Sun, X. Liang, F. Liu, X. Yan, The room temperature gas sensor based on Polyaniline@ flower-like WO3 nanocomposites and flexible PET substrate for NH3 detection, Sensor. Actuator. B Chem. 259 (2018) 505–513.
[24] S. Mani, V. Vediyappan, S.-M. Chen, R. Madhu, V. Pitchaimani, J.-Y. Chang, S.-B. Liu, Hydrothermal synthesis of NiWO4 crystals for high performance non-enzymatic glucose biosensors, Sci. Rep. 6 (2016) 24128.
[25] J. Tian, Y. Xue, X. Yu, Y. Pei, H. Zhang, J. Wang, Solvothermal synthesis of NiWO4 nanostructure and its application as a cathode material for asymmetric supercapacitors, RSC Adv. 8 (2018) 41740–41748.
[26] S. Bai, K. Zhang, R. Luo, D. Li, A. Chen, C.C. Liu, Low-temperature hydrothermal synthesis of WO3 nanorods and their sensing properties for NO2, J. Mater. Chem. 22 (2012) 12643–12650.
[27] N.M. Hung, N.M. Hieu, N.D. Chinh, T.T. Hien, N.D. Quang, S. Majumder, G. Choi, C. Kim, D. Kim, Rb2CO3-decorated In2O3 nanoparticles for the room-temperature detection of sub-ppm level NO2, Sensor. Actuator. B Chem. (2020) 128001.
[28] N.D. Chinh, T.T. Hien, L. Do Van, N.M. Hieu, N.D. Quang, S.-M. Lee, C. Kim, D. Kim, Adsorption/desorption kinetics of nitric oxide on zinc oxide nano film sensor enhanced by light irradiation and gold-nanoparticles decoration, Sensor. Actuator. B Chem. 281 (2019) 262–272.
[29] N.M. Hieu, T.T. Hien, N.D. Chinh, N.D. Quang, N.M. Hung, C. Van Phuoc, S.-M. Lee, J.-R. Jeong, D. Kim, ZnTe-coated ZnO nanorods: hydrogen sulfide nano-sensor purely controlled by pn junction, Mater. Des. (2020) 108628.
[30] J.H. Lehman, M. Terrones, E. Mansfield, K.E. Hurst, V. Meunier, Evaluating the characteristics of multiwall carbon nanotubes, Carbon 49 (2011) 2581–2602 %@ 0008-6223.
[31] M. Piran, V. Kotlyar, D.D. Medina, C. Pirlot, D. Goldman, J.-P. Lellouche, End-selective functionalization of carbon nanotubes. Use of DOE for the optimization of a DNA probe attachment and hybridization using an enzymatic amplifying system, J. Mater. Chem. 19 (2009) 631–638.
[32] J. Guo, Y. Li, S. Zhu, Z. Chen, Q. Liu, D. Zhang, W.-J. Moon, D.-M. Song, Synthesis of WO 3@ Graphene composite for enhanced photocatalytic oxygen evolution from water, RSC Adv. 2 (2012) 1356–1363.
[33] S. Gómez, N.M. Rendtorff, E.F. Aglietti, Y. Sakka, G. Suárez, Surface modification of multiwall carbon nanotubes by sulfonitric treatment, Appl. Surf. Sci. 379 (2016) 264–269.
[34] S. Woo, Y.-R. Kim, T.D. Chung, Y. Piao, H. Kim, Synthesis of a graphene–carbon nanotube composite and its electrochemical sensing of hydrogen peroxide, Electrochim. Acta 59 (2012) 509–514 %@ 0013-4686.
[35] L. Xu, M.-L. Yin, S.F. Liu, Ag x@ WO 3 core-shell nanostructure for LSP enhanced chemical sensors, Sci. Rep. 4 (2014) 6745.
[36] Y.K. Kim, H. Park, Light-harvesting multi-walled carbon nanotubes and CdS hybrids: application to photocatalytic hydrogen production from water, Energy Environ. Sci. 4 (2011) 685–694.
[37] C.H. Lau, R. Cervini, S.R. Clarke, M.G. Markovic, J.G. Matisons, S.C. Hawkins, C.P. Huynh, G.P. Simon, The effect of functionalization on structure and electrical conductivity of multi-walled carbon nanotubes, J. Nanoparticle Res. 10 (2008) 77–88.
[38] G. Halek, I.D. Baikie, H. Teterycz, P. Halek, P. Suchorska-Woźniak, K. Wiśniewski, Work function analysis of gas sensitive WO3 layers with Pt doping, Sensor. Actuator. B Chem. 187 (2013) 379–385.
[39] P. Liu, Q. Sun, F. Zhu, K. Liu, K. Jiang, L. Liu, Q. Li, S. Fan, Measuring the work function of carbon nanotubes with thermionic method, Nano Lett. 8 (2008) 647–651 %@ 1530-6984.
[40] N.S. Ramgir, C.P. Goyal, P.K. Sharma, U.K. Goutam, S. Bhattacharya, N. Datta, M. Kaur, A.K. Debnath, D.K. Aswal, S.K. Gupta, Selective H2S sensing characteristics of CuO modified WO3 thin films, Sensor. Actuator. B Chem. 188 (2013) 525–532.
[41] W. Su, T. Leung, C. Chan, Work function of single-walled and multiwalled carbon nanotubes: first-principles study, Phys. Rev. B 76 (2007) 235413.
[42] P.R. Bandaru, Electrical properties and applications of carbon nanotube structures, J. Nanosci. Nanotechnol. 7 (2007) 1239–1267.
[43] A. Maiti, Bandgap engineering with strain, Nat. Mater. 2 (2003) 440–442.
[44] J.F. Moulder, Handbook of X-ray photoelectron spectroscopy, Physical electronics (1995) 230–232.
[45] A. Antonaia, T. Polichetti, M. Addonizio, S. Aprea, C. Minarini, A. Rubino, Structural and optical characterization of amorphous and crystalline evaporated WO3 layers, Thin Solid Films 354 (1999) 73–81.
[46] W. Shi, X. Zhang, J. Brillet, D. Huang, M. Li, M. Wang, Y. Shen, Significant enhancement of the photoelectrochemical activity of WO3 nanoflakes by carbon quantum dots decoration, Carbon 105 (2016) 387–393.
[47] L.-M. Peng, Z. Zhang, S. Wang, Carbon nanotube electronics: recent advances, Mater. Today 17 (2014) 433–442.
[48] K. Xiao, Y. Liu, P.a. Hu, G. Yu, X. Wang, D. Zhu, High-mobility thin-film transistors based on aligned carbon nanotubes, Appl. Phys. Lett. 83 (2003) 150–152.
[49] Y. Zhao, A. Liao, E. Pop, Multiband mobility in semiconducting carbon nanotubes, IEEE Electron. Device Lett. 30 (2009) 1078–1080.
[50] N.M. Vuong, H. Jung, D. Kim, H. Kim, S.-K. Hong, Realization of an open space ensemble for nanowires: a strategy for the maximum response in resistive sensors, J. Mater. Chem. 22 (2012) 6716–6725.
[51] N.M. Vuong, D. Kim, H. Kim, Surface gas sensing kinetics of a WO3 nanowire sensor: part 1—oxidizing gases, Sensor. Actuator. B Chem. 220 (2015) 932–941.
[52] N.D. Chinh, N.D. Quang, H. Lee, T. Thi Hien, N.M. Hieu, D. Kim, C. Kim, D. Kim, NO gas sensing kinetics at room temperature under UV light irradiation of In2O3 nanostructures, Sci. Rep. 6 (2016) 35066.
[53] N.D. Chinh, C. Kim, D. Kim, UV-light-activated H2S gas sensing by a TiO2 nanoparticulate thin film at room temperature, J. Alloys Compd. 778 (2019) 247–255.
[54] P.-G. Su, S.-L. Peng, Fabrication and NO2 gas-sensing properties of reduced graphene oxide/WO3 nanocomposite films, Talanta 132 (2015) 398–405.
[55] H.W. Kim, H.G. Na, Y.J. Kwon, S.Y. Kang, M.S. Choi, J.H. Bang, P. Wu, S.S. Kim,

Microwave-assisted synthesis of graphene–SnO2 nanocomposites and their applications in gas sensors, ACS Appl. Mater. Interfaces 9 (2017) 31667–31682.
[56] V. Galstyan, E. Comini, I. Kholmanov, G. Faglia, G. Sberveglieri, Reduced graphene oxide/ZnO nanocomposite for application in chemical gas sensors, RSC Adv. 6 (2016) 34225–34232.
[57] R. Leghrib, A. Felten, J.J. Pireaux, E. Llobet, Gas sensors based on doped-CNT/SnO2 composites for NO2 detection at room temperature, Thin Solid Films 520 (2011) 966–970.
[58] G. Varma, Synthesis of CuO-ZnO/rGO ternary composites for superior NO2 gas sensor at room temperature, Mater. Res. Express 6 (2018) 035011.
[59] J.-H. Lee, A. Katoch, S.-W. Choi, J.-H. Kim, H.W. Kim, S.S. Kim, Extraordinary improvement of gas-sensing performances in SnO2 nanofibers due to creation of local p–n heterojunctions by loading reduced graphene oxide nanosheets, ACS Appl. Mater. Interfaces 7 (2015) 3101–3109.